Promoting Fuel Cell Durability and Efficiency Through Air Management System Optimization in Heavy Duty Applications

M P Bunce, N D Peters, H R Blaxill
Dumarey USA
A Taylor, J Wichlinski, P Naik
BMTS Technology US Corporation

1 Abstract

Fuel cell electric vehicles offer an attractive option for decarbonizing long-haul on-road transport. However, there are still several barriers to widespread adoption of hydrogen-fueled fuel cells for this application including system durability and total cost of ownership compared to traditional diesel engines. A primary contributor to fuel cell system costs and maintenance requirements is the air management system. It is common for heavy duty fuel cell electric vehicles to use light-duty automotive air management components which are ill-suited for the requirements of larger, long-haul vehicles. This study focuses on the development of a durable and efficient air management system for heavy duty vehicle applications as part of a cooperative research project funded by the Department of Energy's Hydrogen and Fuel Cell Technologies Office[1].

The proposed air management design incorporates a novel two-stage filtration system, an innovative water-lubricated bearing and electrically-assisted variable turbine geometry turbocharger, charge air cooler, and humidifier. To achieve the project goals for efficiency and durability, a system-level optimization approach has been employed using a semi-empirical 1D model. Design optimization of the compressor and turbine wheel geometries yielded a large compressor wheel diameter and small trim to reduce mass flow capacity, resulting in a broad efficiency map and a relatively small turbine wheel diameter with non-radial inlet blade angle suitable for the low temperature exhaust. 1D simulations of the optimized system compared to a baseline e-compressor showed a >40% reduction in required e-motor power at steady-state conditions and a >30% reduction in e-motor energy consumption in a transient cycle. The results demonstrate how targeted component-level optimization can increase fuel cell system efficiency and enhance durability.

2 Introduction

2.1 Fuel cell propulsion

Transformation of the long-haul Class 8 truck market towards zero emissions is considered a challenging task due to market requirements for long range, low total cost of ownership (TCO), and minimal downtime. With a forecasted 4% yearly rise in vehicle sales in this section of the transportation industry [1], and medium- and heavy-duty (HD) trucks already accounting for one third of on-road greenhouse gas (GHG) emissions [2], it is imperative to find suitable low-emission powertrain solutions for this sector to meet future regulatory GHG targets. Table 1 compares

[1] Financial support for the work detailed in this study was provided by DOE HFTO under Award Number DE-EE0009619.

three proposed powertrain options to replace current diesel internal combustion engines (ICEs) in long haul Class 8 trucks – hydrogen ICE, fuel cell electric vehicle (FCEV), and battery electric vehicle (BEV) [3]. Given the payload advantage and potential for further development, FCEVs are considered a viable option for decarbonizing the HD truck sector [4]. FCEVs, utilizing hydrogen as fuel, offer improved drivetrain efficiency with minimal changes in refueling time and payload capacity compared to diesel ICEs, while maintaining an acceptable vehicle range.

Table 1. Comparison of low- and zero-emission powertrain options for long haul Class 8 trucks [3].

Powertrain	Advantages	Disadvantages
Hydrogen ICE	Low cost, payload, refueling time, range	Drivetrain efficiency, fuel system cost, emissions
FCEV	Payload, refueling time, range, emissions	Capital cost, durability, high-purity H_2, reliability
BEV	Drivetrain efficiency, maintenance, emissions	Capital cost, payload, recharging time

Fuel cells are electrochemical devices wherein each cell exploits the chemical nature of a given fuel to generate electricity in the presence of electrolytes and catalysts. Although various types of fuel cells have been developed, productionized fuel cells generally fall into one of two categories – solid oxide fuel cell (SOFC) and proton exchange membrane (PEM). SOFCs operate at a high temperature, up to 1000°C, and are well suited for combined heat and power applications. Alternatively, PEM fuel cells, which typically operate at approximately 80°C, have emerged as a preferred choice for transportation applications due to their fast start-up time, high power density, and superior load-following capability compared to SOFCs [5].

Presently, PEM fuel cells are commercially available for light-duty applications, with a peak power output of around 100-200 kW [6]. In the architecture of a Class 8 FCEV, multiple fuel cell stacks are strategically combined to achieve a collective power rating of up to 300 kW [7]. Table 2 shows a summary of announced Class 8 FCEVs from several OEMs, typically utilizing two fuel cell stacks to attain the required power.

Table 2. Fuel cell stack power and number of fuel cell stacks for publicized Class 8 FCEV truck demonstrators.

Manufacturer	Stack Output (kW)	Number of Stacks	Range (miles)
Volvo and Mercedes [12]	150	2	620
Kenworth[13]	80	2	450
Hyundai[14]	90	2	250
Navistar [15]	80	Multiple	300+
Quantron[16]	120	2	500+
Nikola [17]	120	2	~500

Despite a push toward higher power fuel cells for HD applications, it is likely that multiple stacks will be required for HD vehicles in the near-term. An issue with the use of multiple smaller fuel cell stacks is an increase in the number of components within the fuel cell system, particularly if each fuel cell stack is supported by its own individual balance of plant (BOP). A PEM fuel cell system comprises a multitude of BOP components which support operation of the fuel cell stack. Figure 1 shows a fuel cell system with the air management system (air compression, filtration, and humidification) and hydrogen supply shaded green, thermal management system (condensers, evaporators, radiators, and pumps) shaded blue, and power electronics shaded yellow. Eventually, a push towards a single high-power fuel cell stack solution will allow for unifying the system BOP, improving overall system efficiency. This will require the scale-up of the fuel cell BOP from light-duty to HD-sized components [8]. Further efficiency improvements are possible through vehicle-level optimization of the powertrain components and energy management calibration [9-11].

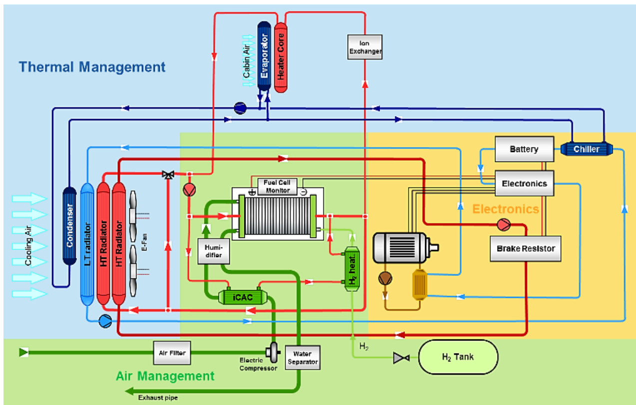

Figure 1. Fuel cell system highlighting various BOP components.

2.2 Challenges with fuel cell system durability

Despite the many advantages of FCEVs, their reliability and durability must be improved to meet the requirements of the Class 8 truck market and provide a competitive TCO versus diesel ICE powertrains. A study by the National Renewable Energy Laboratory (NREL) on fleets using fuel cell electric busses (FCEB) found that FCEBs had the lowest availability among various powertrain options [18]. The FCEB fleet also consistently fell below the target 85% availability rate over a 6-month period of operation, as shown in Figure 2. The fuel cell stack consistently met or exceeded the target availability, with the reliability issues centering around the fuel cell BOP and other vehicle systems. Among those sub-systems, compressors, plumbing, and air blowers have been found to have the most significant impact on FCEB downtime [19]. This highlights the need to develop right-sized, system-level components dedicated for fuel cells that match the robustness expected for a lifetime of operation in on-road HD vehicles.

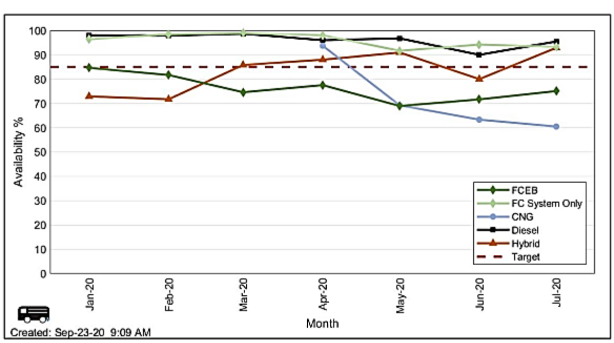

Figure 2. Fuel cell bus fleet availability over a 6-month period compared to other powertrain options [18].

Several types of air compressors can be used for fuel cell applications including mechanical screw compressors, e-superchargers, and centrifugal compressors. For both mechanical screw compressors and e-superchargers, the weight, volume, and efficiency are less favorable than centrifugal compressors. Additionally, they do not give the opportunity for exhaust enthalpy harvesting. Recovery of energy from the exhaust can be achieved with turbochargers, which utilize centrifugal compressors, however, commercially available turbocharger designs have been optimized for ICEs instead of the low temperature fuel cell flow regime. A design-optimized, electrically assisted centrifugal compressor represents an attractive option for a highly efficient fuel cell air compression system. Additionally, incorporation of a turbine optimized for the low exhaust enthalpy can provide a reduction in parasitic losses, improving the net efficiency of the fuel cell system [20,21].

For all fuel cell air compression systems, lubrication poses a challenge. First, there is no oil system on a fuel cell as there is with ICEs, meaning oil lubricated compressors require their own dedicated oil system. Secondly, any oil leaks into the air path from the compressor will contribute to fuel cell stack degradation [22]. Possible alternatives to oil lubricated bearings include air bearings and water-lubricated bearings; the latter is evaluated in this study.

Within the air management system, another key component for promoting durability is the air filter. The fuel cell stack has stringent not-to-exceed requirements for pollutant species found in ambient air. Violating these levels can produce irreversible performance loss as the catalyst materials within the fuel cell stack are poisoned. Figure 3 lists 2021 Environmental Protection Agency (EPA) average measurements of ambient pollutants that are harmful to fuel cell stack performance at the 50th, 95th, and 99th percentiles. The most acute stack damage is caused by the highlighted pollutants: nitrogen oxides (NO_x), ammonia (NH_3), and sulfur dioxide (SO_2).

Discussions with multiple fuel cell stack suppliers and other stakeholders including DOE have indicated that maximum allowable concentrations to prevent long-term degradation to the fuel cell stack are <10 ppb of the described pollutants. The inset table within Fig. 3 shows the required minimum adsorption efficiency of the air filter in order to adhere to the not-to-exceed targets. As evidenced by this figure, ambient pollutant concentrations become a concern in 95th and above percentile regions. Therefore a robust filtration solution incorporating adsorption of these ambient pollutants is necessary for applications such as class 8 long-haul.

Minimum Required Adsorption Efficiency – Primary Filter

	NO_X	NH_3	SO_2
99th Percentile, Max	95.9%	84.2%	99.8%
95th Percentile, Avg	76.9%	48.3%	70.6%

2021 EPA Data – Average / Max of All Sampling Locations

Harmful Gas	CO	CO_2	NO_X	NH_3*	SO_2	Ozone	H_2S	Cations
99th Percentile, Max	25.10 ppm	637.0 ppm	243.0 ppb	19.0 ppb	407.6 ppb	0.112 ppm	30.2 ppb	13.4 μg/m^3
95th Percentile, Avg	0.58 ppm	477.7 ppm	43.2 ppb	5.8 ppb	3.4 ppb	0.065 ppm	1.9 ppb	1.04 μg/m^3
50th Percentile, Avg	0.25 ppm	426.7 ppm	9.1 ppb	2.2 ppb	0.5 ppb	0.045 ppm	0.56 ppb	0.22 μg/m^3

** 2020 EPA Data*

Figure 3. EPA average ambient pollutants in the 50th, 95th, and 99th percentile, and corresponding required minimum adsorption efficiency of a

fuel cell air filter in order to prevent performance degradation of the fuel cell stack under long-term exposure.

3 OBJECTIVE

The work performed in this study is part of an on-going cooperative research project funded by the Department of Energy's Hydrogen and Fuel Cell Technologies Office (DOE HFTO). The agency aims to support research and development to achieve a fuel cell vehicle TCO that is competitive with conventional ICE powertrains. To achieve this goal and improve the uptake of fuel cell vehicles in the marketplace, DOE HFTO has set performance targets for long-haul Class 8 fuel cell trucks at 25,000 hour (1 million miles) durability and a $80/kW fuel cell system cost by 2030 [23].

The fuel cell BOP, and the air management components specifically, are major contributors to system cost, system efficiency (through parasitic losses), and reliability. With a trend towards higher pressure operation of the cathode as fuel cell power densities increase, DOE HFTO has identified air compression systems as a main BOP component requiring further development to improve efficiency and durability.

In this program, DOE HFTO has set technical targets for the air compression systems to improve the uptime, efficiency, durability, and turndown ratio relative to what is currently commercially available for high power HD fuel cells (Table 3). While the goal is an air compression system sized for a 300-kW fuel cell, this size of fuel cell is not currently prevalent. To better match the size of fuel cells being introduced to the market in the coming years, the project team is developing and testing a 2/3rds scale prototype system.

Table 3. DOE HFTO technical targets for the air compression system (of any configuration) for 300-kW HD fuel cells [24].

Characteristic	**Units**	**2030 Targets**
Motor + Motor Controller Efficiency At 100% Flow	%	92
At 50% Flow	%	92
At Idle	%	80
Isentropic Compressor/Expander Efficiency At 100% Flow	%	75/70
At 50% Flow	%	80/80
At Idle	%	62/60
Transient Time for 10-90% of Maximum Flow	seconds	2
Durability (component-specific)	hours	25,000
Reliability	Miles Between Road Calls	50,000
Number of Start-Up and Shutdown Cycles	-	50,000
Noise at Idle	dBa @ 1m	65

System Cost (air compression system)	$/kW net	12
System Volume	L/kW net	0.25
System Weight	kg/kW net	0.50
Turndown Ratio (max/min flow)	-	20

The objective of this work is to develop a durable, efficient, and low-cost air management system capable of achieving the project technical targets. Although the primary focus of the program is on the air compression components, this work considers the entire cathode BOP, as all components in the air path are inextricably linked in terms of performance and durability. Development of the air compression system is therefore coupled with development of a novel air filtration system, having a direct impact on durability by filtering gasses and particulates harmful to the fuel cell stack and an impact on air compressor performance by minimizing pressure losses in the air path.

This study details the design, optimization, and modeling of a water-lubricated variable turbine geometry (VTG) e-turbocharger for high power HD fuel cells and a primary air filter incorporating adsorption of ambient pollutants harmful to the fuel cell stack. The air filter promotes filtration of small particles such as dust and large particles like road salt. Compressor and turbine matching to the specific application is employed routinely for ICE and fuel cell powertrains, and this approach is employed here. The compressor bearing incorporates water lubrication as an alternative to oil lubrication in order to prevent oil contamination in the fuel cell stack due to leakage or catastrophic failure. This presents an advantage over competitive technologies such as screw-type compressors. The water-lubricated bearing also presents a durability and performance advantage over air bearing technologies. The use of a VTG turbine provides additional energy harvesting for increased system efficiency but also presents a controls challenge versus a simple back pressure valve.

Simulations using a 1D model of the air management system are used to compare performance of the optimized e-turbocharger against a baseline state-of-the-industry e-compressor. Future publications will include more details on the rest of the program’s technical scope including secondary air filtration system development, controls strategy development for the cathode BOP components, and testing of the prototype hardware.

4 METHODOLOGY

In this study, simulation tools are used to assist with the development of a novel fuel cell air compression system; a single-stage centrifugal e-turbocharger with VTG for cathode pressure control. A semi-empirical 1D model of a fuel cell system has been developed, focusing specifically on high-fidelity sub-models for components within the air path.

The 1D model is used for component development activities, optimizing them to achieve the efficiency and durability targets outlined in Table 3. A system-level optimization approach has been employed, using the 1D model in an iterative manner as follows:

- provide inputs for component-level simulations,
- incorporate results (outputs) from component-level simulations into the system 1D model,
- perform simulations to show the impact of design changes on system performance,

- provide new boundary conditions back to the component-level simulations for further optimization,

This iterative approach enables simulation-led design optimization of individual components. When the design is complete for any individual component, it is manufactured and validated in a component test rig. The results from this testing are then input back into the model for validation and further design optimization of remaining components as needed.

In this study, a flow bench is utilized to test the filter prototype designs, and this data was input into the 1D model for improved accuracy. Upon completion of the air compression system components, a hot gas test bench was used to evaluate performance.

The simulations used in this study are supported and informed by testing of individual components. Integrated subsystem testing will be performed as part of a subsequent study. Because of this, simulated subsystem results that are presented here should be viewed as indicative.

The following section provides a description of the component sub-models, model inputs, and controls strategy.

4.1 Fuel cell system 1D model

The fuel cell system 1D model has been constructed using GT Power. An image of the model is shown in Fig. 4. With the project focus on the air management system, special attention was paid to developing the cathode side of the fuel cell with more simplified models of both the anode side and thermal management system.

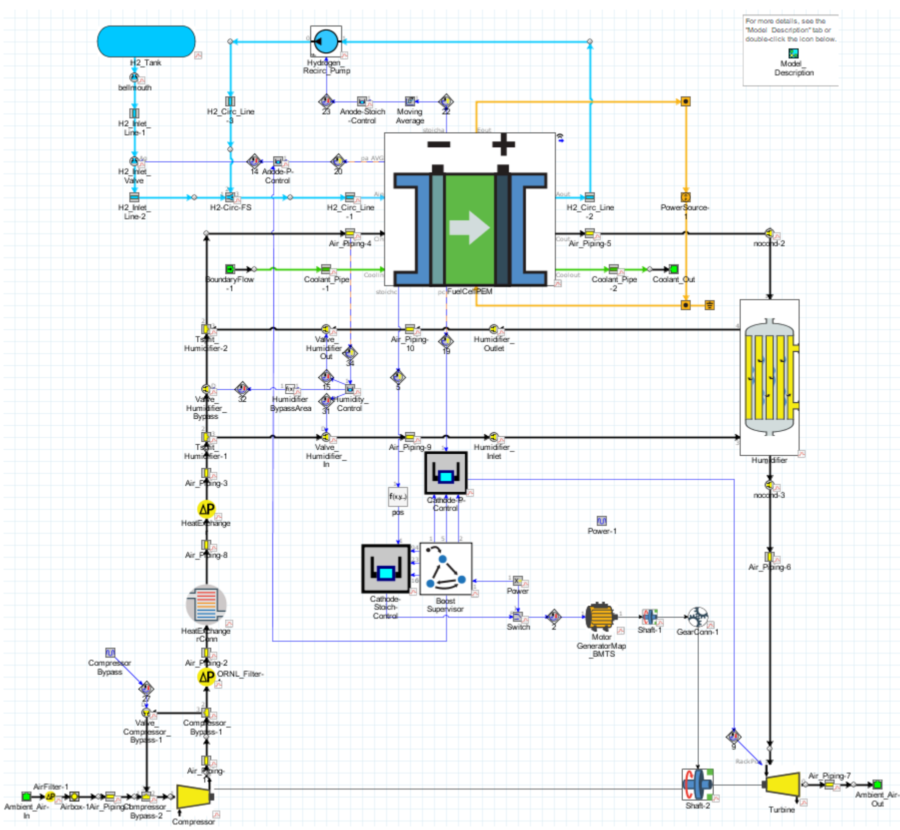

Figure 4. GT Power fuel cell system model used for optimization of air path components.

Inputs for the fuel cell stack model are based on a 2nd generation Toyota Mirai scaled to a rated power of 230 kW [25]. This fuel cell stack was selected as a starting point for the stack model due to its relatively high efficiency among current production PEM fuel cells and the availability of benchmark data. The reference polarization curve was then modified based on industry input to improve its representation of the performance of pre-production 200 kW fuel cell stacks. The Tafel activation loss model is utilized, with the reference polarization curve defined by a set of coefficients. The polarization curve used in the model at reference conditions of 70°C and a relative humidity (RH) of 80% is presented in Fig. 5. This polarization curve corresponds to a single cell. The use of dynamic models for exchange current density, ohmic resistance, and diffusion allow the stack model to be used in a quasi-predictive manner at varying operating conditions. Cathode manifold and channel dimensions were altered, modifying the cathode pressure loss to improve agreement with target pressure loss values at idle, 50% power, and 100% power based on feedback from industry. Heat generation through losses within the fuel cell stack are modeled along with heat transfer to anode, cathode, and coolant fluids. Membrane water content is modeled using a steady solver.

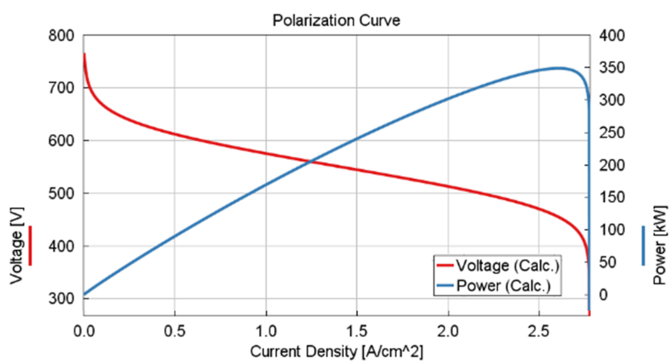

Figure 5. Polarization curve used in the fuel cell system 1D model at reference conditions of 70°C and 80% RH.

Coolant supply to the fuel cell is modeled as a constant coolant flow rate and temperature, representative of warm, steady-state operation, and is held constant at each load point. Future updates to the model will include a more detailed thermal management model to more accurately capture heat transfer within the fuel cell during start-up and cold operation. Similarly, the intercooler in the air path uses a simple heat exchanger model imposing a temperature and calculating the energy required to achieve the target temperature.

The anode supply circuit is represented by the light blue lines in Fig. 4 and consists of a hydrogen fuel tank, supply valve, and recirculation pump. The supply valve is controlled by a proportional-integral-derivative (PID) controller and adjusted to achieve the desired power output. Anode stoichiometry is controlled by the recirculation pump.

Semi-empirical models are used for several components within the air path using internal test data. Pressure drop through the air filter is imposed using data tables of pressure drop versus flow rate. The model then calculates a loss coefficient and Reynolds number, enabling the performance to be extrapolated to other temperatures and flow rates outside the domain of the test data.

A gas-to-gas humidifier model is incorporated into the inlet and exhaust paths. Using an internally developed 0D simulation tool correlated to humidifier test data, performance data generated for a representative humidifier was used to tune the GT Power humidifier model. A bypass valve is used to control humidity of the air to the cathode. Thermal effects are captured in the humidifier model. A water separator has not been incorporated in the system upstream of the turbine inlet. An emphasis is placed on developing a durable turbine design capable of withstanding water droplet impingement, eliminating the need for the water separator and thereby eliminating its cost.

The turbocharger model comprises a compressor, electric motor, turbine, and shaft connecting the components. The compressor model calculates performance of the compressor by interpolating within a user-defined map. Power for the compressor is provided by the e-motor and a VTG. The VTG model uses a best-fit equation to user-defined performance maps for each rack position to smooth the data and extrapolate to the edges of the map. Rack position is selected by the cathode pressure controller. The e-motor also uses a user-defined map to calculate performance with model inputs coming from test data of the selected e-motor.

The pressure controller for the cathode side attempts to maintain a target pressure at the fuel cell stack inlet manifold. The pressure is modulated by controlling the VTG rack position which alters the backpressure in the fuel cell exhaust stream – e.g., a more closed VTG position will increase backpressure which in turn increases the fuel cell stack inlet pressure. The cathode stoichiometry controller attempts to achieve a target stoichiometric ratio in the fuel cell stack. The stoichiometric ratio is the total oxygen flow rate divided by the rate of oxygen consumption within the fuel cell. To achieve a higher stoichiometric ratio, and therefore air flow rate, e-motor power is increased to drive a larger airflow through the compressor. PID controllers are used for both pressure and stoichiometric ratio control in the model.

Targets for the cathode pressure and stoichiometric ratio controllers at the three operating points of interest were selected through review of fuel cell studies and benchmark data and refined based on industry feedback. Selected key parameters of fuel cell operation (cathode pressure, air stoichiometry) and design (cathode pressure differential) are summarized in Fig. 6. The values for these operating conditions at idle, 50%, and full load are represented by symbols. These parameters were developed in consultation with industry partners as appropriate average values for a fuel cell system of this size and application. The largest change with load occurs for the cathode stoichiometric ratio. A high stoichiometric ratio is used at low power conditions to improve cell stability, for water management within the fuel cell stack, and to support a compressor design that achieves high efficiency across the load span considered in this study. In practice, these values will vary depending on fuel cell design and for a given stack they will vary depending on environmental conditions. The operating conditions used in this model are intended to represent normal operation of a state-of-the-industry high power fuel cell.

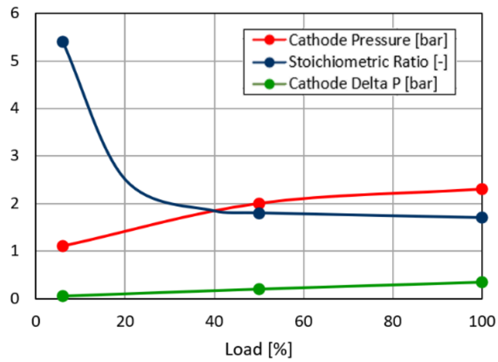

Figure 6. Select parameters for fuel cell operation specific to the air path – cathode pressure, air stoichiometric ratio, and cathode pressure differential. Parameters are plotted versus fuel cell load with symbols representing idle, 50% power, and 100% power conditions. Pressure is absolute.

4.2 Model assumptions

The fuel cell system 1D model was created to assist with development of the air management system. Due to the nature of this study, the model includes several simplifying assumptions for components and sub-systems which were not a focus of the program (e.g., fuel cell stack, thermal management system, anode supply). The following list details several of these assumptions with an explanation of their impact on model accuracy and simulation results.

- The fuel cell stack polarization curve is not directly correlated to test data from a 200-kW fuel cell. Any deviations from the modeled stack efficiency would have a direct impact on the mass air flow requirement at a given operating condition, influencing the compressor and expander efficiencies. Additionally, the uncorrelated dynamic behavior of the fuel cell stack model means it may under or overpredict the fuel cell stack response to cathode operating conditions (pressure, temperature, stoichiometric ratio, RH) deviating from the target values during transients. The main impact is on stack outlet conditions, influencing both humidifier and turbine performance.

- A simplified thermal management model is used where coolant temperature boundary conditions are prescribed for the charge air cooler and fuel cell stack. The fuel cell net (system) power therefore only accounts for power consumption from the air management system. Additionally, although a dynamic fuel cell stack thermal model is utilized, the static coolant inlet temperature means system response to changing thermal boundary conditions is not captured. Colder coolant temperatures during warm-up would lower the fuel cell stack exhaust temperature, reducing the energy recuperated by the turbine and thus increasing the e-motor power requirement.

- The turbine map used for aerodynamic matching is based on empirical models from ICE applications where the exhaust temperature, and therefore heat loss, is considerably higher than with a fuel cell. As will be explained in the subsequent section, computational fluid dynamics (CFD) modeling was used to improve the turbine performance prediction. However, experimental results are needed to confirm the turbine efficiency with the low enthalpy fuel cell exhaust which will be a focus of future work on this project.

• A full transient controls strategy and calibration has not been developed for the fuel cell model. This will be incorporated in a future phase of the project. While not required for the back-to-back comparison of the two air compression systems in this study, the lack of refined transient controls does leave room for further optimization of the system to reduce power consumption of the e-compressor during transients.

• Stop-start and other vehicle considerations have not been incorporated into the model because they are out of scope of the program.

5 Results

For a fuel cell system, it is important to ensure that no contamination enters the fuel cell stack via air supply. This necessitates the use of oil free bearings such as gas foil bearings [22]. The fuel cell compressor investigated here is equipped with a novel water lubricated bearing system. The lubricant employed is a mixture of 50 % water and 50% glycol. This bearing, shown in Fig. 7, is a water lubricated variant of the BMTS 3D bearing used in automotive turbocharger applications [26]. The bearing uses the existing coolant circuit. There is an associated pressure drop but this is minor and therefore has minimal impact on the coolant system power requirement. The 3D bearing is a semi-floating ring bearing with outer squeeze film damper which resists both radial and thrust loads. The bushing is held in position by a fixation pin which also acts as the lubricant inlet. The 3D bearing contour is designed as a segmented surface. The smooth transition from radial to axial bearing surfaces maintains the pressure and allows for a smaller diameter axial bearing to be used, as shown in Fig. 8. Compared to a traditional air bearing, this reduces frictional losses from 325 W to 210 W.

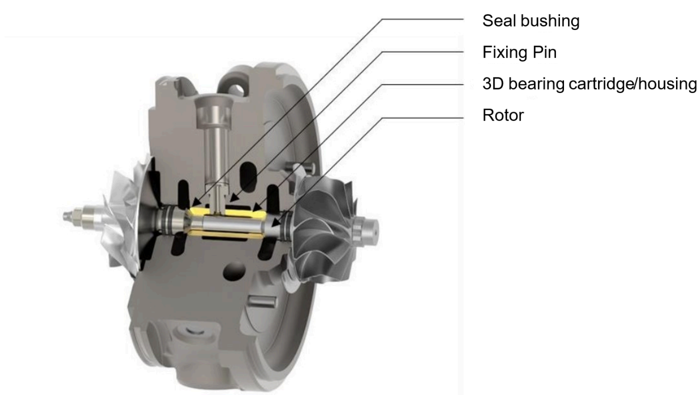

Figure 7. Core unit showing 3D bearing [26].

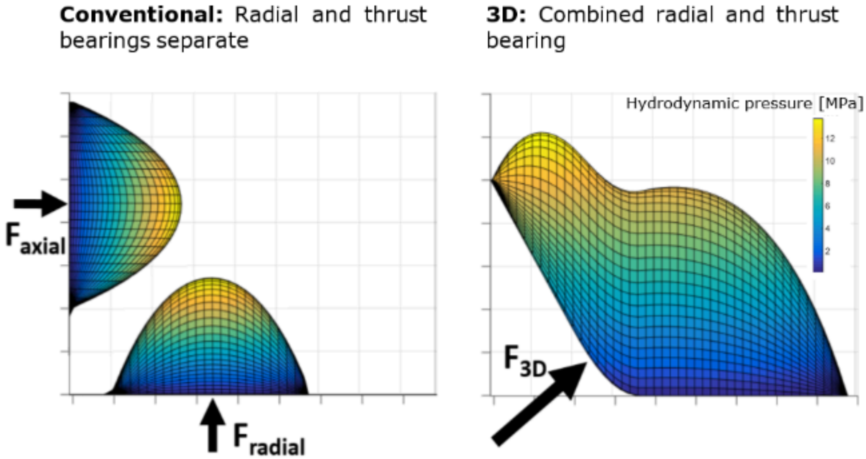

Figure 8. Fluid film pressure in 3D bearing compared to a conventional bearing. Hydrodynamic pressure corresponds to an operating point. X-axis is bearing axial direction, y-axis is bearing radial direction [26].

The bearing system employed here is investigated for its functionality and durability for up to 130,000 revolutions per minute (RPM). The investigation is performed in multiple stages, starting with a conventional system without an electric motor. With such a configuration, the system was evaluated over speeds ranging from 10,000 RPM to 130,000 RPM. During this study, the mass flow was varied from surge to choke to estimate the functionality and reliability of the system. Further, the boundary conditions at the coolant inlet and outlet were varied with primary focus on the bearing longevity. It was found that the setup was able to maintain stable operation throughout the tests. Coolant inlet temperatures from 0 C to 90 C were evaluated.

5.1 Turbocharger optimization

Aerodynamic matching of the turbocharger was performed utilizing the fuel cell operating conditions of air mass flow, target compressor outlet pressure, and turbine inlet pressures provided by the fuel cell system 1D model. These operating conditions are shown on the compressor and turbine maps in Fig. 9 and Fig. 10, respectively. Considerations for the compressor sizing include surge margin, or sufficient margin to compressor surge, and speed margin, the distance from the operating point’s speed to the compressor choke line. High shaft speeds are necessary to generate high pressure ratios, however, from a bearing durability and sealing perspective, lower shaft speeds are preferred. A compromise was found in utilizing a large diameter compressor wheel for high tip velocities and therefore high pressure ratio capability, but with an unorthodox small trim to reduce mass flow capacity of the large compressor wheel. The selected compressor wheel diameter is 82 mm with 53% trim.

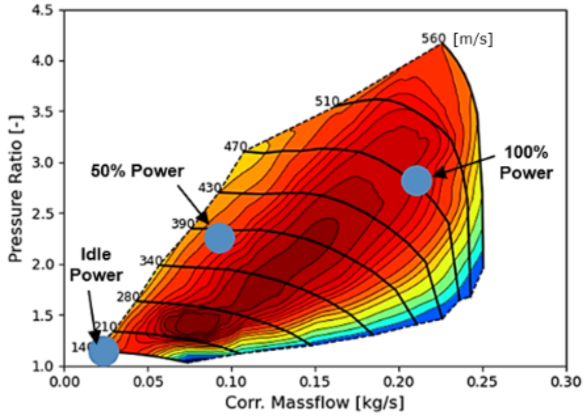

Figure 9. Fuel cell operating points plotted on the compressor map.

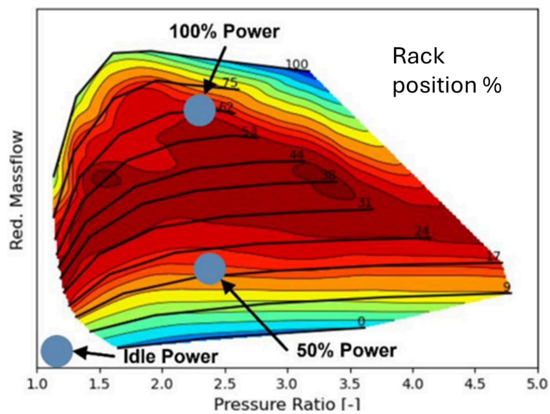

Figure 10. Fuel cell operating points plotted on the turbine map.

On the turbine stage, consideration was given to the low fuel cell exhaust temperature, in the range of 90°C, relative to a typical gasoline engine application of 950°C. Due to low exhaust gas temperatures in the fuel cell environment, specific mass flow capacity demanded of the turbine stage is reduced as described by the turbine mass flow parameter (MFP). MFP is defined in Equation 1 where $\dot{m}$ is the mass flow, T_3 is the turbine inlet temperature, and P_3 is the turbine inlet pressure.

$$MFP = \dot{m} * \frac{\sqrt{T_3}}{P_3} \tag{1}$$

The optimum turbine wheel diameter, 44 mm, is smaller than the typical turbine wheel diameter given the compressor wheel size. For ICE applications, compressor wheel to turbine wheel diameter ratio is 1.1 to 1.2 which would yield a larger turbine wheel diameter between 68 mm and 75 mm for the selected 82 mm compressor wheel.

CFD-based aerodynamic optimizations were performed on both the compressor wheel and turbine wheel stages, with both the wheel and housing designs optimized. The optimizations were carried out utilizing a numerical optimization approach, where the optimizer was run to optimize two different fuel cell operating points for both the compressor and the turbine. The outline of the optimization workflow is as follows: A parametrized geometry model is set up within Ansys Workbench™ where it is connected to Ansys TurboGrid™ for Meshing and CFX® for flow simulation. This CFD workflow is coupled with Ansys optiSLang™ to perform the optimization based on a genetic algorithm. The optimizer generated and analyzed more than 1000 designs each, from which a pareto front was generated and a few optimal designs were selected. It was possible to increase the efficiency in the desired operating points, with potential for further optimization during the hardware test phase planned in the near future.

The result of the design optimization efforts is summarized in Table 4. The values here represent the efficiency improvement with the optimized design as predicted by CFD-based simulation tools. These values will be confirmed with physical hardware in the next phase of the project. The compressor efficiency improved by 1 percentage point at all operating points with the potential for an additional 1–3 percentage point improvement dependent on experimental results on the test stand. Figure 11 shows the predicted efficiency improvement versus mass flow at three different pressure ratios for two candidate designs compared to the baseline design. As is observed, the improvements in efficiency are concentrated at lower flow conditions.

Table 4. Compressor and turbine wheel optimization results.

Wheel	Operating point	Efficiency of optimized design (percentage point improvement)
Compressor	Idle	+1 %-point
	50% power	+1 %-point
	100% power	+1 %-point
Turbine	Idle	+4 %-point
	50% power	+4 %-point
	100% power	+2 %-point

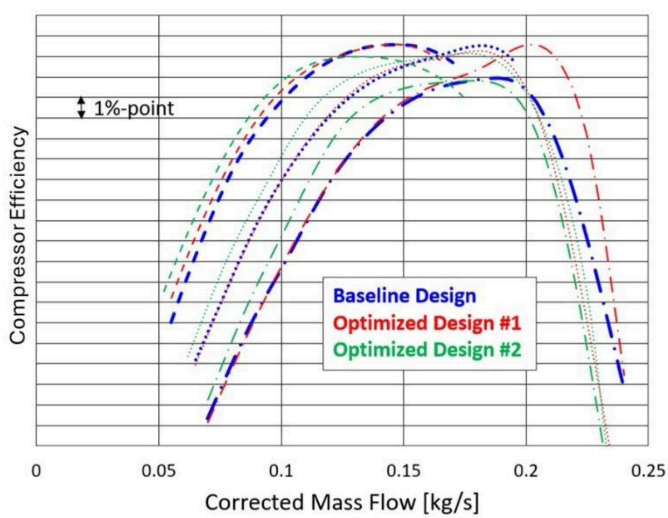

Figure 11. Normalized predicted compressor efficiency versus mass flow at three different pressure ratios (dashed line, dotted line, dash-dotted line).

Optimized designs refer to compressor wheel and housing designs tailored to achieving performance targets.

A larger efficiency improvement of up to 4 percentage points was observed for the turbine side design optimization which resulted in a non-radial inlet blade angle. This type of design is possible due to the low exhaust temperatures of around 90°C, compared to 950°C and above for automotive ICE applications where the radial blade inlet angle is necessary to mitigate thermal fatigue and creep issues. Figure 12 shows the efficiency improvement versus mass flow achieved with the optimized turbine design at the idle condition.

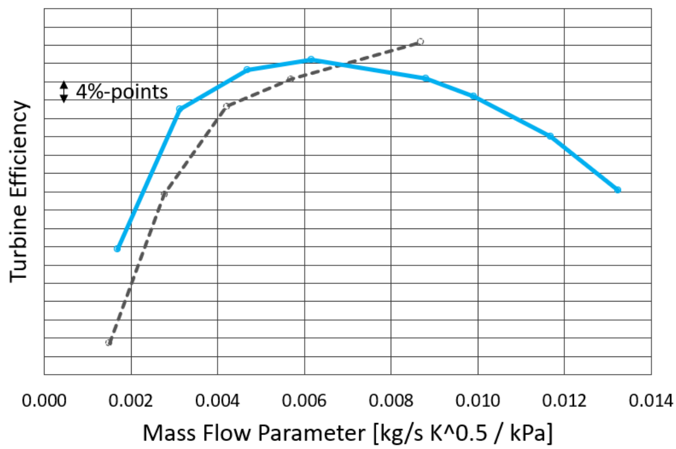

Figure 12. Example of predicted turbine efficiency improvement at the idle operating condition with the optimized turbine (solid line) versus the baseline (dashed line).

5.2 **Filter**

The air filter was sized for the intended fuel cell capacity and application, with an emphasis on minimizing pressure drop, thereby reducing the strain on the compressor and maximizing its efficiency. The filter design is shown in Fig. 13. Two filter designs were evaluated at a nominal air flowrate of 12 m^3/min and pressure loss was determined at various rated flowrates. As is displayed in Fig. 14, both filter designs registered a pressure loss of approximately 6 mbar, which translated to a maximum pressure loss of approximately 10 mbar for the full filter assembly (air cleaner and filter element). This was well within the project target and compared favorably to state-of-the-art filtration solutions for high power fuel cells.

Figure 13. CAD model of filter housing (left) and cross section showing filter (right).

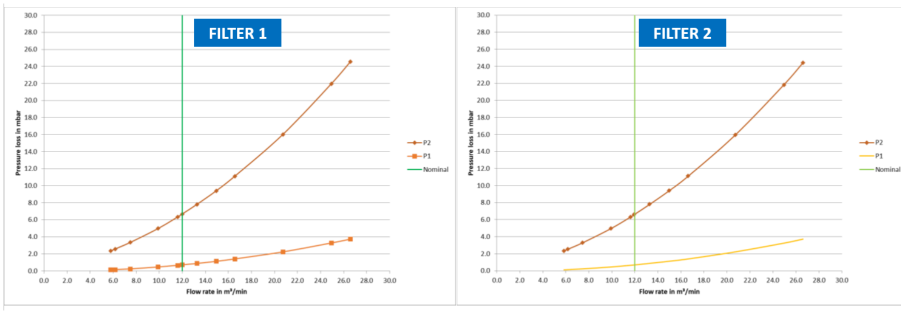

Figure 14. Pressure loss vs. flow rate for two filter tests. P1 and P2 correspond to pressure sampling at upstream and downstream filter positions, respectively.

The filtration components represent approximately 50% of the air compression system volume and approximately 25% of the air compression system weight.

A simulated filter pressure drop was used as input to the 1D system model in order to help inform the design of the compressor. The filter is not regenerated, and so pressure drop steadily increases over product lifetime. The model result was then updated and validated according to the filter test results, and simulation-led compressor design was finalized. Future work will focus on demonstrating the adsorption efficiency of the filter and determination of the filter replacement interval.

5.3 **Fuel cell system 1D simulations**

Following the completion of the design phase of the optimized fuel cell air compression and filtration system, the 1D fuel cell system model described in the methodology was updated with the optimized compressor and turbine maps shown in Fig. 9 and Fig. 10, respectively. Simulations utilizing this model were used for assessing the system's performance under realistic operating conditions for vehicle applications.

Another version of the fuel cell system 1D model was created with a baseline air compression system, selected as a basis for comparing and evaluating the performance of the optimized system. The baseline system is a commercially available compressor, designed for ICE applications, configured as an e-compressor. In order to focus the performance comparison only on turbocharger design, the e-motor map from the optimized system was carried over and used on the baseline system as well. Cathode pressure for the baseline system was controlled by a backpressure valve in the exhaust pipe. Specifications of the baseline system and the optimized system developed in this study are summarized in Table 5.

Table 5. Specifications for the baseline and optimized air compression systems used in the fuel cell system 1D model.

Characteristic	Baseline System	Optimized System
System type	e-Compressor	e-Turbo
Compressor Size	70 mm	82 mm
Compressor Maximum Corrected Flow Rate	0.31 kg/s	0.26 kg/s
Turbine Size	N/A	44 mm
Cathode Pressure Control	Backpressure Valve	VTG

In the following sections, results from steady-state and quasi-static simulations are presented. Henceforth "baseline system" refers to the commercial e-compressor and "optimized system" refers to the e-turbocharger developed through this study.

5.4 Steady state simulations

Steady-state simulations were carried out at the three operating points in the project technical targets (Table 3) which are idle, 50% power, and 100% power. Figure 15 shows the percentage point difference in compressor efficiency between the optimized and baseline compressors. At 100% power, the efficiency difference between the optimized and baseline compressors is 2.2 percentage points. This comes from the high compressor efficiency achieved in the optimized system through aerodynamic optimization simulations in pursuit of the project technical targets.

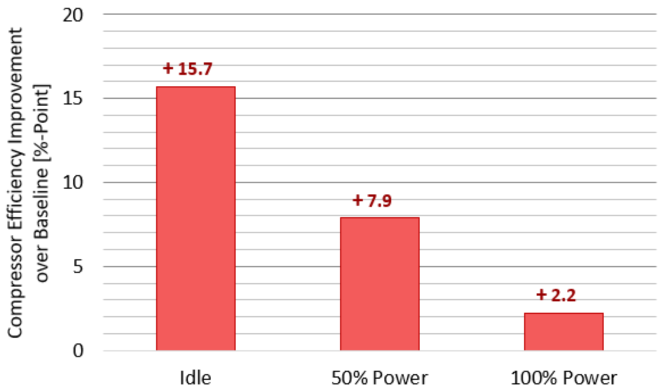

Figure 15. Percentage point efficiency improvement with optimized compressor versus baseline compressor at three steady-state operating points, from CFD results.

The efficiency improvement over the baseline compressor increases as load is decreased with a 7.9 percentage point and 15.7 percentage point increase at 50% power and idle, respectively. Peak isentropic efficiency increases from 73% in the baseline design to 79.3% in the optimized design. This improvement is a culmination of the aerodynamic matching efforts, detailed in the preceding section, to tailor this specific compressor design to the application by selecting a large compressor wheel trimmed for reduced mass flow. The error in the model-based compressor efficiency prediction is largest for the idle condition due to the location of that operating point in the far bottom left corner of the compressor map. Here, extrapolation may be required depending on the data available for a given compressor. Additionally, at idle, small perturbations in the operating condition (i.e., pressure ratio, mass flow) and environmental conditions (i.e., inlet temperature, pressure) can lead to a large change in compressor efficiency. For these reasons it should be expected that the experimentally observed compressor efficiency difference at idle may differ from the model-based prediction.

A benefit of the increased compressor efficiency is a reduction in parasitic losses through the e-motor, improving the fuel cell system efficiency. The red bars in Fig. 16 show the e-motor electrical power for the optimized system normalized by the e-motor power for the baseline system at the three steady-state operating conditions. The e-motor power is normalized in order to account for the impact of the efficiency increase due to the compressor design and turbine addition. In general, the e-motor power for the optimized system was approximately 55% of the required e-motor power for the baseline system. The reduction in required e-motor power has two sources: one is the compressor efficiency improvement and the other is the inclusion of a turbine in the optimized system. The relative contribution of these two sources changes significantly with load as shown in Fig. 16 where the green bars represent the turbine power contribution and the blue bars represent the reduction in e-motor power coming from the higher compressor efficiency with the optimized system. At idle, 12% of the reduction in e-motor power compared to the baseline system comes from the inclusion of the turbine and 34% comes from the compressor efficiency improvement. This is the operating point with the greatest compressor efficiency improvement, as was shown in Fig. 15, and the lowest exhaust enthalpy. At 100% power the result is reversed, with the turbine contributing to 33% of the e-motor power reduction and the compressor efficiency improvement contributing 11%.

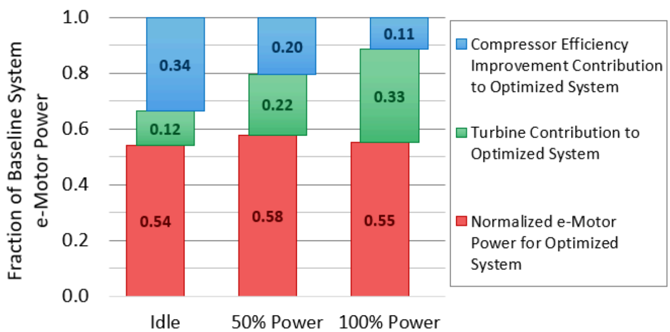

Figure 16. E-motor electrical power for the optimized system (red) normalized by the baseline system e-motor power. Green and blue sections represent the power reduction due to contributions from the turbine and the compressor efficiency improvement, respectively.

Through the inclusion of the turbine and improvement in compressor performance, a significant reduction in parasitic losses to the air management hardware was achieved with the optimized system at steady-state conditions. The e-motor power consumption in the optimized system remained well below 10% of the fuel cell gross power across the entire range of operating conditions. This does not hold true for the baseline system, particularly at high loads where the required air mass flow rate is high and no exhaust energy is recuperated.

5.5 **Quasi-static simulations**

Transient performance of the air compression system was assessed by subjecting the quasi-static 1D fuel cell system model to the load demand from a transient emission cycle. The load profile selected was from the engine-based HD Federal Test Procedure (HD-FTP). The HD-FTP is a transient cycle for emissions certification of HD on-road engines. The cycle is defined in terms of normalized engine speed and torque. For this simulation, these values were combined to define a required power to satisfy the transient cycle and denormalized using the fuel cell stack gross power of 230 kW. This assumes a case where the fuel cell is the primary motive force for the vehicle with minimal contribution from a battery pack. Incorporating a full powertrain model in future work will improve the system efficiency prediction by more accurately representing the transient fuel cell load in a HD vehicle.

The fuel cell's required power throughout the HD-FTP cycle is shown in the top plot of Fig. 17, where gross power was held constant in order to isolate the benefit from the compressor and expander. The idle power used in the transient cycle is identical to the idle condition in the steady-state simulations, approximately 5% of full power. The bottom plot of Fig. 17 shows the percentage point improvement in compressor efficiency with the optimized system over the baseline system. As was observed in the steady-state results, the compressor efficiency improvement is nearly 16 percentage points during the idle portions of the transient cycle. At high loads, the efficiency improvement drops to < 5 percentage points over the baseline compressor. Several points throughout the transient cycle drop to negative values representing a baseline compressor efficiency greater than the optimized compressor even though no steady-state conditions captured this behavior. These minimums occur briefly during decelerations where the fuel cell gross power quickly reduces. The discrepancy in compressor efficiencies comes from the slower response in pressure control with the VTG of the optimized system compared to the backpressure valve on the baseline system. The baseline system therefore passes through the efficiency island as mass flow is reduced where the optimized system passes through a less efficient region of the compressor map. Future work on optimization of the cathode mass flow and pressure controls strategy with the VTG e-turbocharger is expected to resolve this issue.

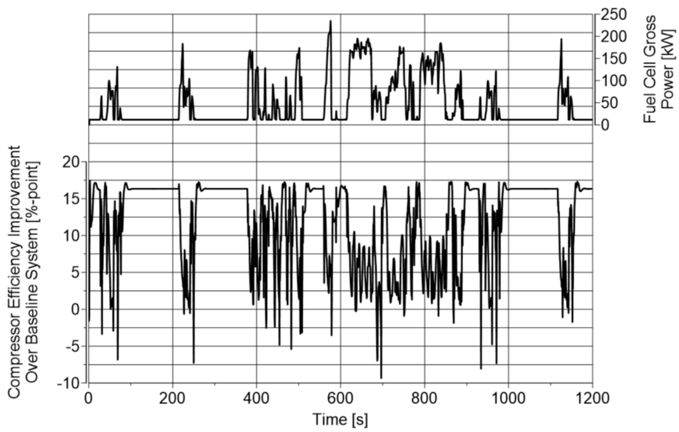

Figure 17. [Top] Fuel cell gross power during the simulated HD-FTP transient cycle. [Bottom] Percentage point improvement in compressor efficiency with optimized compressor versus the baseline compressor.

Figure 18 shows the cycle integrated e-motor energy for the optimized system in red, normalized by the cumulative e-motor energy across the transient cycle for the baseline system. The reduction in energy consumption across the cycle due to the inclusion of the turbine and due to the compressor efficiency improvements for the optimized system are shown in green and blue, respectively. The results are presented in a similar manner to the steady-state results in Fig. 16. A summary of the cumulative and cycle average results is also presented in Table 6. The cycle-average power was 44kW.

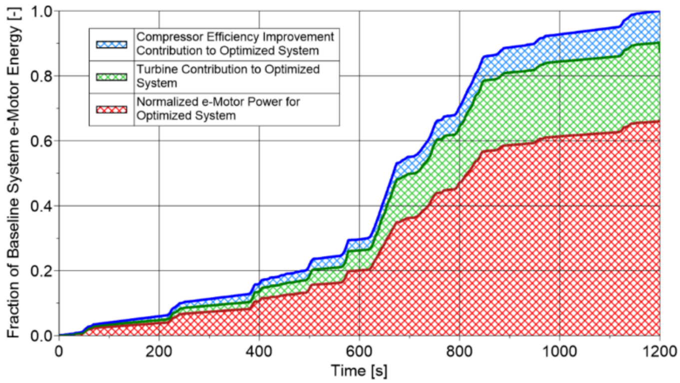

Figure 18. E-motor energy across the HD-FTP transient cycle for the optimized system (red) normalized by the baseline system e-motor energy. Green and blue sections represent the energy reduction due to contributions from the turbine and the compressor efficiency improvement, respectively.

Table 6. Summary of cycle-average and cumulative results from the HD-FTP transient cycle comparing optimized and baseline system performance.

	Cycle Results with Optimized System
Cycle average fuel cell power, normalized by peak fuel cell power	19.2 %
Cycle average compressor efficiency improvement over baseline system	11.8 %-points
Transient cycle **e-motor electrical energy**, normalized by baseline system e-motor energy	66.0 %
Transient cycle **turbine energy**, normalized by baseline system e-motor energy	21.3 %
Compressor efficiency improvement contribution to e-motor energy reduction	12.7 %

The transient cycle results show a couple of key differences from the steady-state results. First, the e-motor power for the optimized system was less than 58% of the e-motor power for the baseline system at all of the steady-state points considered. However, in the transient cycle, the cumulative e-motor energy of the optimized system was 66% of the baseline system. This is due to the e-motor's use at the start of each load step to achieve the target mass flow rate, leading to higher energy consumption from the e-motor relative to the steady-state conditions where the balance in power contribution between the e-motor and turbine stabilizes. Second, based on the cycle-average fuel cell power of 19.2% of full load power, the steady-state results show that the split in relative contribution to the e-motor power reduction between compressor efficiency improvement and turbine contribution should favor the compressor at lower loads. However, the transient cycle results show that the turbine contributes more to the e-motor energy reduction, 21.3% of the baseline system e-motor energy, compared to a 12.7% contribution from the compressor efficiency improvement over the baseline system. This offset from the steady-state results can be attributed in part to the decelerations in the transient cycle where exhaust enthalpy momentarily remains high relative to the fuel cell power as load is reduced.

Future work will focus on improvements to the control strategy for the optimized system and evaluation of start-up and shutdown behavior through simulation with the fuel cell system 1D model. The ability of the system to control to the target operating conditions during transient operation and the impact that deviations from these conditions have on system efficiency will be investigated. Testing of the system with the optimized e-turbocharger integrated with the rest of the air management BOP will take place on a gas test stand, with a digital twin of the fuel cell stack imitating its response to operating conditions via real-time simulations. The test work evaluating the optimized hardware and validating the simulation results described in this study will be the focus of forthcoming publications.

6 CONCLUSIONS

This study describes the design, optimization, and simulation of a centrifugal e-turbocharger and primary air filter for HD fuel cell applications. The air filter incorporates adsorption capability to promote fuel cell stack durability. Future work will quantify the adsorption capability of the air filter within the context of the EPA ambient pollutant levels. The e-turbocharger uses a novel water-lubricated 3D bearing to prevent oil contamination of the fuel cell stack and a VTG for pressure control of the cathode air supply. The 3D bearing design minimizes frictional losses and, with water lubrication, shows reduced radial oscillation of the rotor shaft when compared with an oil lubricated bearing through rotor dynamic simulations. Preliminary endurance tests confirmed functionality of the seal design and displayed no unusual signs of wear on the bearing. A 1D model of the fuel cell system was constructed, focusing specifically on the air path. The model was used to provide inputs for hardware development and evaluation of the optimized system at realistic operating conditions. Using inputs from the 1D model, aerodynamic matching of the turbocharger was performed. CFD-based simulation tools were used for further wheel and housing design optimization. The optimized compressor design was a large wheel diameter of 82 mm and small trim to reduce mass flow capacity, resulting in a broad efficiency map. The optimized turbine design was a 44 mm wheel diameter with non-radial inlet blade angle suitable for the low temperature exhaust. Steady-state and quasi-static simulations were performed using the fuel cell system 1D model, comparing the optimized e-turbocharger VTG design with a commercially available e-compressor and exhaust backpressure valve.

Steady-state simulations showed a > 40% reduction in required e-motor power with the optimized system at all operating conditions. The magnitude of the relative contribution of the higher compressor efficiency and inclusion of a turbine to the reduction in e-motor power with the optimized system was highly dependent on the fuel cell load. Simulation results from an HD-FTP transient cycle showed a reduction in the improvement over the baseline system in terms of e-motor power. Additionally, a higher relative contribution from the turbine was observed in the transient cycle when compared to the steady-state simulations. These results will be used to help guide further controls optimization of the air management system, particularly during transient operation. The simulation results will be validated against test results of the assembled air management BOP system in an upcoming phase of the project using a novel virtual fuel cell development platform.

Multiple design considerations promoted durability in the system. These include selection of water impingement-resistant materials and coatings for the turbine, pipe routing to prevent water build-up in the turbine housing, water lubrication for the compressor bearing, and the use of a dual-filtration approach to promote stack durability. The durability of these individual components will be quantified in a future study.

7 References

1. "Long-distance general freight trucking market - global industry analysis, size, share, growth, trends, regional outlook, and forecast 2023-2032," Precedence Research, August 2023.
2. United States Environmental Protection Agency, "Fast Facts: U.S. Transportation Sector Greenhouse Gas Emissions 1990 – 2021," EPA-420-F-23-016, 2023.
3. Basma, H., Buysse, C., Zhou, Y., and Rodríguez, F., "Total cost of ownership of alternative powertrain technologies for Class 8 long-haul trucks in the United States," 2023.
4. Cunanan, C., Tran, M.K., Lee, Y., Kwok, S. et al., "A Review of Heavy-Duty Vehicle Powertrain Technologies: Diesel Engine Vehicles, Battery Electric Vehicles, and Hydrogen Fuel Cell Electric Vehicles," Clean Technologies 3, no. 2 (2021): 474-489, doi:10.3390/cleantechnol3020028.
5. Mat, Z.B.A., Kar, Y.B., Hassan, S.H.B.A. and Talik, N.A.B., "Proton Exchange Membrane (PEM) and Solid Oxide (SOFC) Fuel Cell Based Vehicles-a Review," in 2017 2nd IEEE International Conference on Intelligent Transportation Engineering (ICITE), Singapore, 2017, pp. 123-126, doi:10.1109/ICITE.2017.8056893.
6. Enomoto, K., Ida, A., Harada, T., and Takeuchi, H., "Development of Safety Performance for FC Stack in the New Toyota FCEV," SAE Technical Paper 2022-01-0686 (2022), doi:10.4271/2022-01-0686.
7. Kelly, K., Bennion, K., Miller, E., and Prohaska, B., "Medium- and Heavy-Duty Vehicle Duty Cycles for Electric Powertrains," No. NREL/PR-5400-66228, National Renewable Energy Lab (NREL), Golden, CO (United States), 2016.
8. Qiu, Y., Zeng, T., Zhang, C., Wang, G. et al., "Progress and Challenges in Multi-Stack Fuel Cell System for High Power Applications: Architecture and Energy Management," Green Energy and Intelligent Transportation 2, no. 2 (2023): 100068, doi:10.1016/j. geits.2023.100068.
9. Tran D.-D., Hegazy O., Van Mierlo J., Klüppel Smijtink R., et al., "Modeling and Co-design Optimization for Heavy Duty Trucks," in In The 31st International Electric Vehicles Symposium and Exhibition, EVS31, 2018.
10. Ferrara, A., Zendegan, S., Koegeler, H.-M., Gopi, S. et al., "Optimal Calibration of an Adaptive and Predictive Energy Management Strategy for Fuel Cell Electric Trucks," Energies 15 (2022), doi:10.3390/en15072394.
11. Sorrentino, M., Bevilacqua, G., Bove, G., and Pianese, C., "Simulation-Based Assessment of Fuel Economy Performance in Heavy-Duty Fuel Cell Vehicles," SAE Technical Paper 2023-24-0146 (2023), doi:10.4271/2023- 24-0146.
12. "Volvo Trucks Showcases New Zero-Emissions Truck." Volvo Trucks has started tests of fuel cell electric trucks., June 20, 2022. https://www.volvotrucks.com/en-en/ news-stories/press-releases/2022/jun/volvo-truckshowcases-new-zero-emissions-truck.html.
13. "T680 Fuel Cell Electric Vehicle." Kenworth Trucks. https://www.kenworth.com/trucks/t680-fcev/.
14. "Xcient Fuel Cell Truck." Hyundai Electrified Commercial Vehicles. https://ecv.hyundai.com/global/en/products/ xcient-fuel-cell-truck-fcev/
15. "Hydrogen Fuel Cell: Navistar." Hydrogen Fuel Cell | Navistar. https://www.navistar.com/our-path-forward/ hydrogen-fuel-cell.
16. "Quantron QHM FCEV for Emission-Free Transportation." Quantron, October 18, 2023. https:// www.quantron.net/en/q-truck/q-heavy/qhm-fcev/.
17. "The Hydrogen Fuel Cell Electric Class 8 Vehicle" - Nikolamotor.com. http://www.nikolamotor.com/wp-content/uploads/2023/09/FCE022_FCEV_Brochure_Full_09.25.2023.pdf.

18. Eudy, L. and Post, M., "Fuel cell buses in U.S. Transit Fleets: Current Status 2020," No. NREL/TP-5400-75583, National Renewable Energy Lab (NREL), Golden, CO (United States), 2021, doi:10.2172/1772437.
19. Wang, G., Miller, M., and Fulton, L., "Estimating Maintenance and Repair Costs for Battery Electric and Fuel Cell Heavy Duty Trucks," 2022.
20. Taylor, A.H., Naik, P., Nibler, S., and Al-Hasan, N.S., "Comparison of Efficient Boosting Technologies for Fuel Cell Applications," in 44th International Vienna Motor Symposium, Austria, 2023.
21. Taylor, A.H., Naik, P., Nibler, S., and Al-Hasan, N., "Optimization of Variable Geometry Turbine Electric Turbocharger for a Heavy-Duty, on-Highway Fuel Cell," Turbo Expo: Power for Land, Sea, and Air 87110 (2023): V13DT34A004, doi:10.1115/GT2023-101224.
22. Filsinger, D., Kuwata, G., and Ikeya, N., "Tailored Centrifugal Turbomachinery for Electric Fuel Cell Turbocharger," International Journal of Rotating Machinery 1-14 (2021), doi:10.1155/2021/3972387.
23. Papageorgopoulos, D., 2023 Annual Merit Review and Peer Evaluation Meeting (Washington, DC: U.S. Department of Energy Hydrogen and Fuel Cell Technology Office, June 2023)
24. "Hydrogen and Fuel Cells R&D 2021 FOA", U.S Department of Energy Office of Energy Efficiency and Renewable Energy, DE-FOA-0002446, 2020.
25. Yoshizumi, T., Kubo, H., and Okumura, M., "Development of High-Performance FC Stack for the New MIRAI," SAE Technical Paper 2021-01-0740 (2021), doi:10.4271/2021- 01-0740.
26. Kleinschmidt, R., Schmitt, S., Stetter, F., Kuhne, O. et al., "The Future Bearing Concept of BMTS Technology," in 19. Internationales Stuttgarter Symposium, 2019, doi:10.1007/978-3-658-25939-6_61.